Title	Unusual elasticity of monoclinic β-Ga2O3
Author(s)	Adachi, K.; Ogi, H.; Takeuchi, N. et al.
Citation	Journal of Applied Physics. 2018, 124(8), p. 085102-1-085102-7
Version Type	VoR
URL	https://hdl.handle.net/11094/84235
rights	This article may be downloaded for personal use only. Any other use requires prior permission of the author and AIP Publishing. This article appeared in Journal of Applied Physics, 124(8), 085102 (2018) and may be found at https://doi.org/10.1063/1.5047017.
Note	

Unusual elasticity of monoclinic $\beta-Ga_2O_3$

K. Adachi,[1] H. Ogi,[2,a)] N. Takeuchi,[2] N. Nakamura,[3] H. Watanabe,[4] T. Ito,[4] and Y. Ozaki[4]

[1]*Faculty of Science and Engineering, Iwate University, Morioka, Iwate 020-8551, Japan*
[2]*Graduate School of Engineering, Osaka University, Suita, Osaka 565-0871, Japan*
[3]*Graduate School of Engineering Science, Osaka University, Toyonaka, Osaka 560-8531, Japan*
[4]*Correlated Electronics Group, Electronics and Photonics Research Institute, National Institute of Advanced Industrial Science and Technology (AIST), Tsukuba, Ibaraki 305-8565, Japan*

This paper determines all the 13 elastic constants C_{ij} of monoclinic β-Ga$_2$O$_3$, which has never been achieved since the discovery of this crystal about 100 years ago. We used resonant ultrasound spectroscopy with laser-Doppler interferometry, where the resonant-mode identification was unambiguously made by comparing measured and calculated displacement distributions on the vibrating specimen surface. Using more than 110 resonance frequencies, we inversely determined the C_{ij}: $C_{11} = 242.8 \pm 2.9$, $C_{22} = 343.8 \pm 3.8$, $C_{33} = 347.4 \pm 2.5$, $C_{44} = 47.8 \pm 0.2$, $C_{55} = 88.6 \pm 0.5$, $C_{66} = 104.0 \pm 0.5$, $C_{12} = 128 \pm 0.1$, $C_{13} = 160 \pm 1.5$, $C_{23} = 70.9 \pm 2.1$, $C_{15} = -1.62 \pm 0.05$, $C_{25} = 0.36 \pm 0.01$, $C_{35} = 0.97 \pm 0.03$, and $C_{46} = 5.59 \pm 0.69$ GPa. We also performed a density-functional-theory calculation and found that the local density approximation yields both the lattice parameters and C_{ij} closer to the measurements than the generalized gradient approximation. Strong elastic-stiffness anisotropy is found in the diagonal elastic constants: C_{11} is smaller than C_{22} and C_{33} by ∼30%, and the difference between C_{44} and C_{66} exceeds 50%. Our measurements also reveal anomalous Poisson's ratios: ν_{21} and ν_{31} exceed 0.5, and ν_{23} and ν_{32} are almost zero. We explain these unusual elastic properties with the truss-like deformation of the tetrahedra-octahedra network and confirm this view with the *ab- initio* calculation. *Published by AIP Publishing.*
https://doi.org/10.1063/1.5047017

I. INTRODUCTION

β-Ga$_2$O$_3$ has received intense interest because of its characteristic crystallographic structure and the second widest bandgap among semiconductors. Since its discovery in 1925,[1] there are many reports on the physical properties of β-Ga$_2$O$_3$ until now,[1–11] such as detailed crystal structure,[4] Brillouin zone and band structure,[9] and anisotropic thermal conductivity.[11] However, no study reports the elastic constants C_{ij} of β-Ga$_2$O$_3$ including experiment and theory, despite the discovery of this crystal about 100 years ago;[1] this fact is surprising because β-Ga$_2$O$_3$ is currently highly promising material for power devices, for which the elastic constants are required in designing.

β-Ga$_2$O$_3$ shows very high breakdown electric field (higher than that of GaN by a factor of 2.5)[12] and very large Baliga's figure of merit[13] (larger than that of GaN by a factor of 4), being a desirable power-device material.[12,14–17] Another advantage over GaN is its low manufacturing cost: A β-Ga$_2$O$_3$ monocrystal bulk can be, in principle, synthesized by a melt-growth method,[18,19] allowing large production at lower cost. It is well recognized that the C_{ij} of a power-device material are significantly important in designing the device, because they are indispensable to evaluate the stress field in the device caused by thermal process and lattice misfits with other materials.[20–23] The absence of C_{ij} is, therefore, a critical problem for the applications of β-Ga$_2$O$_3$.
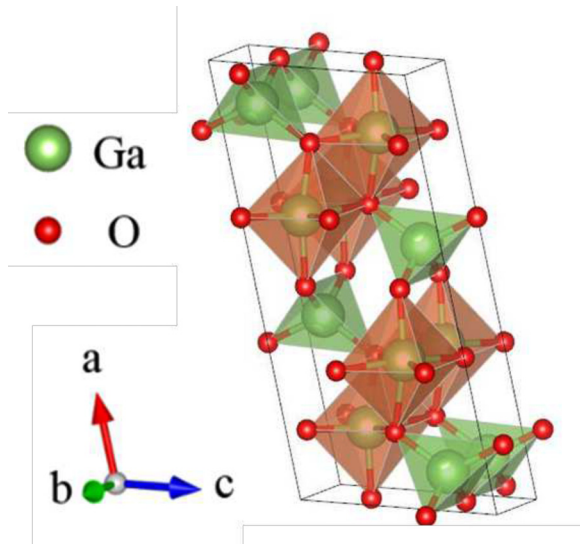
This study determines the complete set of C_{ij} of β-Ga$_2$O$_3$ for the first time. The monoclinic β-Ga$_2$O$_3$ belongs to space group $C2/m$ and shows a crystal structure in which tetrahedra and octahedra are joined by oxygen atoms as shown in Fig. 1. Complete description of its elasticity requires 13 independent C_{ij}

$$[C_{ij}] = \begin{bmatrix} C_{11} & C_{12} & C_{13} & 0 & C_{15} & 0 \\ & C_{22} & C_{23} & 0 & C_{25} & 0 \\ & & C_{33} & 0 & C_{35} & 0 \\ & & & C_{44} & 0 & C_{46} \\ sym. & & & & C_{55} & 0 \\ & & & & & C_{66} \end{bmatrix}.$$

Measuring all the C_{ij} of β-Ga$_2$O$_3$ with conventional methods, such as the plate-thickness resonance method[24] and the pulse-echo method,[25] is a formidable task, where one must acquire at least 13 labyrinthine simultaneous equations through measurements on many specimens with different crystallographic orientation and solve them. It would be, however, difficult to complete such measurements because single-crystal and high-quality specimens are limited to small size.

In this study, we use resonant ultrasound spectroscopy coupled with laser-Doppler interferometry (RUS/LDI)[26–30] to accurately determine all the 13 C_{ij} of β-Ga$_2$O$_3$. This method detects many free-vibration resonant frequencies with a piezoelectric needle tripod and identifies their resonance modes by measuring displacement distributions on the

a)ogi@prec.eng.osaka-u.ac.jp

FIG. 1. The conventional unit cell of β-Ga$_2$O$_3$.

the lattice is also reproduced with the DFT calculation, and we reveal that the truss-like deformation with the tetrahedra-octahedra crystallographic network consistently explains the anomalous elasticity.

II. MEASUREMENTS

Three rectangular-parallelepiped specimens (specimens A–C) were cut from a single-crystal β-Ga$_2$O$_3$ ingot. Table I shows their dimensions. We take the x_1, x_2, and x_3 axes, the three orthogonal principal axes for the monoclinic system as follows: x_2 and x_3 axes are along the b and c axes, respectively, and the x_1 axis is taken to be perpendicular to the x_2–x_3 plane. (Note that the x_1 axis is not parallel to the a axis because the angle between the a and c axes is not $90°$ but $103.7°$ for β-Ga$_2$O$_3$.[3]) The dimensions L_1, L_2, and L_3 denote the side lengths along the x_1, x_2, and x_3 axes, respectively. The mass density determined from mass and dimensions was $5709\,kg/m^3$.

We used the tripod-type RUS/LDI measurement system, whose details appear elsewhere.[26–28] The specimen is put on the tripod consisting of two needle piezoelectric transducers for excitation and detection of acoustic vibrations and one needle just for support. This measurement setup enables ideal free vibrations of the specimen because the external force acting on the specimen is only gravity. This setup allows us to rigorously compare measured resonance frequencies with computed free-vibration values, which dramatically improves the accuracy of the C_{ij} determination. We measured the resonance frequencies of the three specimens up to 2 MHz.

vibrating specimen surface with LDI and comparing them with the theoretical distributions, leading to unambiguous mode identification. The determined C_{ij} show unusual properties, including significantly smaller C_{11} than the other longitudinal moduli, much smaller C_{44} than C_{66}, and unusual Poisson's ratios (some exceed 0.5 and others are nearly zero).

To confirm these elastic properties, we evaluated the C_{ij} using the density-functional-theory (DFT) calculation. The calculated C_{ij} essentially agree with our measurements, reproducing the unusual elastic properties. Deformation of

TABLE I. Dimensions L_i (mm), elastic constants C_{ij} (GPa) of the three β-Ga$_2$O$_3$ specimens, and the rms errors between measured and calculated resonance frequencies after convergence of the inverse calculation. Lattice parameters a, b, and c (Å) and C_{ij} calculated with first-principles calculation, where the local-density-approximation (LDA), the generalized-gradient-approximation (GGA) potential, Becke's three-parameter hybrid exchange functional, and Lee, Yang, and Parr correlation functional (B3LYP) or the hybrid functional of Heyd, Scuseria, and Ernzerhof (HSE) was used.

|	Measurement				Calculation			
	Specimen A	Specimen B	Specimen C	Ref. 3	LDA (this study)	GGA	B3LYP[5]	HSE[9]
L_1	3.021	3.449	3.872					
L_2	5.438	4.454	4.676					
L_3	3.469	3.778	3.661					
a				12.23	12.20	12.51	12.34	12.27
b				3.04	3.04	3.10	3.08	3.05
c				5.80	5.81	5.92	5.87	5.82
C_{11}	240.7	240.8	246.9		219	204		
C_{22}	349.1	341.3	340.9		365	324		
C_{33}	345.0	350.9	346.3		344	305		
C_{44}	48.1	47.8	47.7		54	45		
C_{55}	87.9	88.9	89.1		76	73		
C_{66}	103.5	104.6	103.8		99	93		
C_{12}	128.2	128.3	128.4		127	116		
C_{13}	160.4	158.0	161.6		169	139		
C_{23}	72.0	72.7	68.0		106	78		
C_{15}	−1.68	−1.59	−1.58		−1.4	−1.3		
C_{25}	0.36	0.35	0.35		3.5	2.1		
C_{35}	0.97	1.00	0.93		18	17		
C_{46}	5.89	4.64	6.25		13	7.8		
rms error (%)	0.36	0.35	0.28					
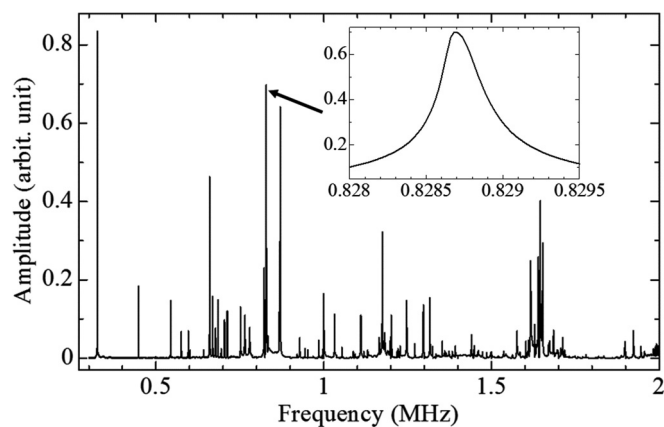
FIG. 2. Resonance spectrum of β-Ga$_2$O$_3$ specimen (specimen B) measured by the RUS system. The inset shows an enlarged resonant peak.

After the resonance-frequency measurements, a 100-nm aluminum film was deposited on the x_2–x_3 face of the specimen. This deposition is necessary to apply laser-Doppler interferometry to β-Ga$_2$O$_3$ because it is a transparent material. The differences of resonance frequencies before and after the deposition were ~0.03%; hence, the mode correspondence is clear even after the aluminum-film addition. We then measured normal-displacement distributions of the surface with laser-Doppler interferometry for mode identification. A Doppler interferometer detects the frequency shift of a reflected beam from the resonating surface and derives the vertical component of the displacement velocity at a focal point. It is possible to gain vertical-velocity distributions, that is, normal-displacement distributions by scanning the whole surface.
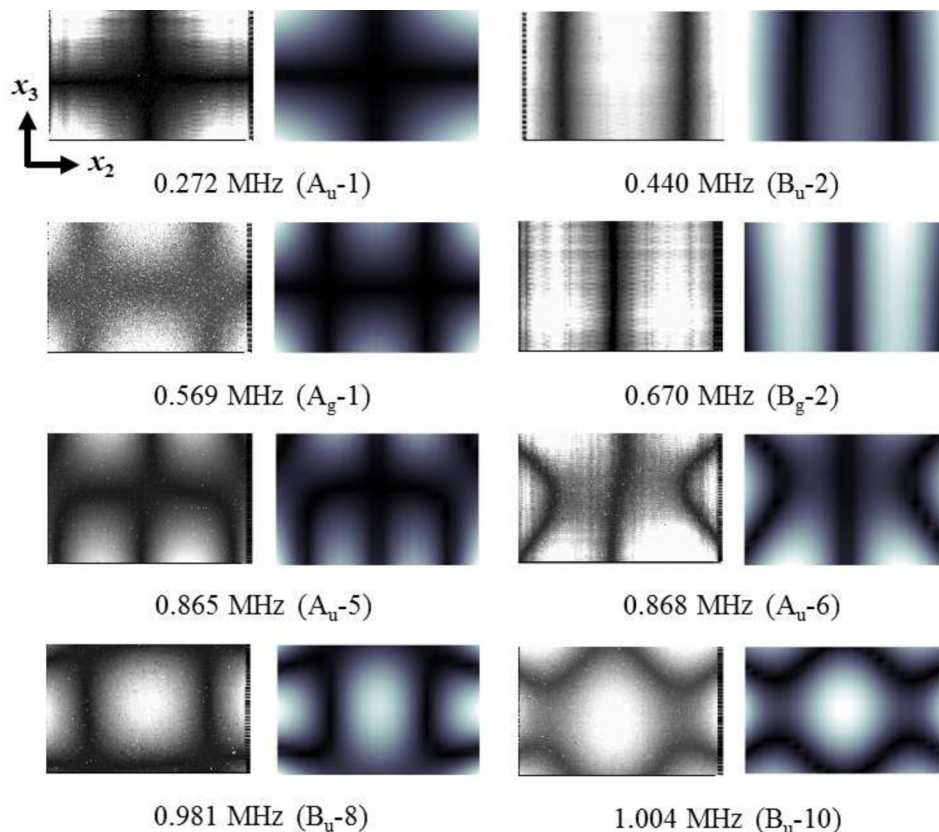
III. RESULTS

Figure 2 shows an example of the measured resonance spectrum of specimen B. The resonance frequency of each resonant mode was obtained by Lorentzian-function fitting procedure. Figure 3 shows examples for comparison between the measured and calculated displacement distributions. Their strong agreement indicates that the visual approach permits unambiguous resonant-mode identification. We identified more than 110 resonant peaks for each specimen and determined all 13 C_{ij} by the inverse calculation: We used normalized Legendre polynomials[31] up to order 24 as the basis functions (~3000 basis functions were used for each displacement). Considering the vibrational symmetry, the free vibrations of the monoclinic-symmetry rectangular parallelepiped fall into four vibrational groups,[31,32] for which the resonance frequencies are separately calculated.

Table I shows inversely determined C_{ij} of the three specimens together with the rms errors between measured and calculated frequencies after convergence; the errors were less than 0.36%.

Also, we estimated the C_{ij} of β-Ga$_2$O$_3$ with *ab-initio* calculation based on density-functional theory. The Vienna *ab-initio* simulation package (VASP)[33] was used. The local density approximation (LDA) and the generalized gradient approximation (GGA) were used to describe the exchange correlation potential. The plane-waves cutoff energy was set to 1300 eV with $10 \times 10 \times 10$ mesh k points. We applied 13 different deformation modes (elongation, shearing, breathing, and so on) to the unit cell up to $\pm 1\%$ in each deformation mode, relaxed the ions inside the cell at individual strain, and calculated the relationship between the total

FIG. 3. Examples of measured (left) and calculated (right) displacement distributions of specimen A. The x_2 and x_3 axes are parallel to the horizontal and vertical axes, respectively. Bright and dark zones represent antinode and node, respectively. The mode denotations follow Mochizuki.[32]

energy and strain. By fitting a harmonic function to the total energy vs. strain curve, we determined the effective stiffness in each deformation mode. All the independent C_{ij} were then obtained.[34–36] The resultant lattice parameters and C_{ij} are given in Table I together with lattice parameters previously reported.[3,5,9]

IV. DISCUSSION

Figure 4 shows the contribution of each elastic constant to resonance frequencies f, defined as $|(C_{ij}/f)(\partial f/\partial C_{ij})|$. This represents the magnitude of frequency change caused by the C_{ij} change. Therefore, C_{ij}, whose contributions are relatively high, are sensitive to the resonance frequencies, and they can be accurately determined by the inverse calculation. The diagonal elastic constants and two off-diagonal elastic constants (C_{12} and C_{13}) should be obtainable with high precision by the inverse calculation because their contributions are large. Indeed, the standard deviations of these elastic constants among the three specimens are less than 1.2%. The measurements of these elastic constants show good agreements with the theoretical values with LDA rather than with GGA (Table I); the rms error between the measurements and the DFT calculations was within 8%. Table I indicates also that the LDA potential provides lattice parameters closer to the measurements[3] (within 0.25% error) than the GGA potential. Thus, the DFT calculation with LDA will be more appropriate for predicting other material properties than with GGA for β-Ga$_2$O$_3$.

From the measured C_{ij}, we determined Young's moduli E_i along the three principal directions, Poisson's ratios ν_{ij} ($= -s_{ij}/s_{ii}$, where s_{ij} denote components of the compliance matrix), and the bulk modulus B as shown in Table II. These results reveal unusual elastic properties: (1) very strong Young-modulus anisotropy ($E_1 \ll E_2, E_3$) as well as strong longitudinal-modulus anisotropy ($C_{11} \ll C_{22}, C_{33}$), (2) very strong shear-modulus anisotropy ($C_{44} \ll C_{55}, C_{66}$), (3) Poisson's ratios exceeding 0.5 (ν_{21} and ν_{31}), and (4) nearly zero Poisson's ratios (ν_{23} and ν_{32}). We find that very similar elastic anomalies appear in θ alumina (θ-Al$_2$O$_3$), which shows the same space group ($C2/m$) as β-Ga$_2$O$_3$. On the other hand, other monoclinic materials with different space

group fail to show the anomalies as shown in Table II; they show normal Poisson's ratios (0.1–0.4) and insignificant elastic anisotropies in Young's and shear moduli. These observations highly indicate that the anomalous elastic properties of β-Ga$_2$O$_3$ result from the specific space group $C2/m$, that is, the polyhedral-linkage structure shown in Fig. 1. β-Ga$_2$O$_3$ and θ alumina show larger bulk modulus than the others, indicating higher binding energy in the tetrahedra-octahedra crystallographic network.

The strong anisotropy in the longitudinal modulus $C_{11} \ll C_{22}, C_{33}$ or $E_1 \ll E_2, E_3$ means that β-Ga$_2$O$_3$ is softer along the x_1 axis. We attribute this elastic anisotropy to the polyhedral-linkage structure. Figures 5(a)–5(c) project the crystal structure of β-Ga$_2$O$_3$ onto the $x_2 - x_3$, $x_1 - x_3$, and $x_1 - x_2$ planes, respectively. β-Ga$_2$O$_3$ has a truss-like structure in which the rigid tetrahedra and octahedra are connected by sharing the vertex or side. They are expected to show high stiffness, that is, high resistance to the change in the neighboring Ga-O bond distance and O-Ga-O bond angle constituting them. Although uniaxial elongation basically requires the increase in the interatomic distance, apparent tensile deformation can arise from the bending of connection between the tetrahedron and octahedron in the x_1 direction. As a result, it is possible to produce the longitudinal deformation along the x_1 axis with less Ga-O bond distance change in the rigid polyhedra, resulting in lower C_{11} than the other longitudinal moduli. To confirm this interpretation, we calculated the atomic migration in β-Ga$_2$O$_3$ caused by the principal tensile and shear strain with the *ab-initio* calculation with LDA. The applied strains are 1%, and the atoms inside unit cell are relaxed. Figure 6 shows the examples of computed atomic behavior. The change ratios of the neighboring Ga-O bond distance of the tetrahedron and octahedron are given in Table III. The calculations reveal that the bond distance change needed to produce the 1% tensile strain in the x_1 direction is smaller than in the x_2 and x_3 direction by $\sim$18%.

As for the principal shear moduli, C_{44} is remarkably small, less than 50% of C_{66}. The shear deformation essentially requires bond angle change because it is necessary to deform without volume change. However, since the square sides of the octahedra are parallel to the x_2 and x_3 axes, the shear deformation in the $x_2 - x_3$ plane will be achieved with less angle change of the rigid O-Ga-O bond by changing into a parallelogram as shown in Fig. 6(b), yielding lower C_{44}. As can be seen in Table III, the *ab-initio* calculation actually demonstrates that the smaller angle change than that in the $x_1 - x_2$ plane (related to C_{66}) by $\sim$38% can produce the equivalent shear deformation in the $x_2 - x_3$ plane (related to C_{44}), supporting our view.

We find a negative elastic constant C_{15}. Since the a axis is inclined against the x_1 axis as shown in Fig. 5(b), the shear strain in the $x_1 - x_3$ plane caused by a tensile stress along the x_1 axis decreases the angle between x_1 and a axes, that is, the shear angle. As a result, C_{15} can become negative.

As mentioned above, β-Ga$_2$O$_3$ shows the following unusual Poisson's ratios: ν_{21} and ν_{31} are larger than 0.5 and ν_{23} and ν_{32} are nearly zero. From Figs. 5(b) and 5(c), it can be seen that β-Ga$_2$O$_3$ includes parallelogram-shape units surrounded by two tetrahedra and two octahedra in the $x_1 - x_3$
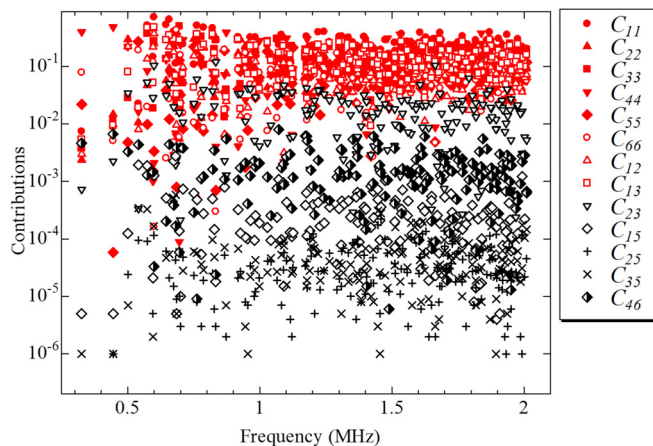

FIG. 4. Normalized contributions of elastic constants to resonance frequencies $|(C_{ij}/f)(\partial f/\partial C_{ij})|$ for specimen B.

TABLE II. Elastic constants C_{ij} (GPa), Young's modulus E_i along the x_i axis (GPa), Poisson's ratios ν_{ij}, the bulk modulus B (GPa), and the Debye temperature Θ_D (K) of monoclinic materials. The isotropic-approximation longitudinal modulus $\langle C_L \rangle^{iso}$ (GPa), the bulk modulus $\langle B \rangle^{iso}$ (GPa), Young's modulus $\langle E \rangle^{iso}$ (GPa), shear modulus $\langle G \rangle^{iso}$ (GPa), and Poisson's ratio $\langle \nu \rangle^{iso}$ are obtained from the averaged-over-direction C_{ij}. The averages of the three specimens are shown.

Space group	β-Ga$_2$O$_3$ (this study) $C2/m$	θ-Al$_2$O$_3$ Ref. 39 $C2/m$	Diopside (CaMgSi$_2$O$_6$)[37] $C2/c$	Hedenbergite (CaFeSi$_2$O$_6$)[38] $C2/c$	Chrome diopside (CaMgCr$_{0.02}$Si$_2$O$_6$)[31] $C2/c$
C_{11}	242.8 ± 2.9	283.8	223	222	228.1
C_{22}	343.8 ± 3.8	420.4	171	176	181.1
C_{33}	347.4 ± 2.5	435.3	235	249	245.4
C_{44}	47.8 ± 0.2	86.8	74	55	78.9
C_{55}	88.6 ± 0.5	104.3	67	63	68.2
C_{66}	104.0 ± 0.5	124.5	66	60	78.1
C_{12}	128 ± 0.1	119.3	77	69	78.8
C_{13}	160 ± 1.5	159.8	81	79	70.2
C_{23}	70.9 ± 2.1	83.0	57	86	61.1
C_{15}	−1.62 ± 0.05	−30.7	17	12	7.9
C_{25}	0.36 ± 0.01	12.3	7	13	5.9
C_{35}	0.97 ± 0.03	16.7	43	26	39.7
C_{46}	5.59 ± 0.69	23.8	7.3	−10	6.4
E_1	141.2 ± 1.5	191.1	174	185	185.3
E_2	275.1 ± 3.5	363.8	140	137	147.7
E_3	241.2 ± 4.0	333.7	179	191	195.3
ν_{12}	0.29 ± 0.005	0.23	0.37	0.28	0.37
ν_{13}	0.40 ± 0.008	0.34	0.25	0.21	0.20
ν_{21}	0.57 ± 0.003	0.43	0.29	0.21	0.29
ν_{23}	−0.057 ± 0.008	0.02	0.15	0.27	0.17
ν_{31}	0.69 ± 0.005	0.59	0.25	0.22	0.21
ν_{32}	−0.050 ± 0.007	0.02	0.20	0.38	0.23
B	182.6 ± 0.3	202.7	108	117	113.4
Θ_D	562 ± 0.6	860	673	609	700
$\langle C_L \rangle^{iso}$	289.7 ± 0.01	348.6	202	203	213.4
$\langle B \rangle^{iso}$	183.1 ± 0.3	204.9	113	120	116.4
$\langle E \rangle^{iso}$	209.3 ± 0.4	275.1	168	158	180.7
$\langle G \rangle^{iso}$	79.9 ± 0.2	107.8	67.1	61.8	72.8
$\langle \nu \rangle^{iso}$	0.31 ± 0.001	0.28	0.25	0.28	0.24

and $x_1 - x_2$ planes. These unit structures function as a square truss, whose Poisson's ratio nearly equals unity when uniaxial stress is diagonally applied, so that Poisson's ratios in these planes become larger. The first-principles calculation indicates the behavior of the parallelogram-shape units as a square truss as shown in Figs. 6(c) and 6(d). Besides, the uniaxial stress applied along the x_2 or x_3 axis easily induces the transverse strain in the x_1 direction because of smaller C_{11}, resulting in larger ν_{21} and ν_{31} values. For these reasons, ν_{21} and ν_{31} can exceed 0.5.

We attribute the nearly zero Poisson ratios (ν_{23} and ν_{32}) to the distinguishing alignment of the tetrahedra in the x_2–x_3 plane seen in Fig. 5(a); two vertices of the tetrahedron lie on the x_2 axis and the other two lie on the x_3 axis as shown in Fig. 5(d). Because the two sides (AB and CD) are orthogonal, an elongation of one side affects little the deformation of the other side. Supplementary material confirms this with an FEM calculation, where an isotropic tetrahedron is elongated along one side, giving almost no change in the length of the other side. Thus, a tetrahedron elastic body inherently shows nearly zero Poisson's ratio when it is uniaxially deformed along the side.

Finally, we calculate the Debye temperature Θ_D through the following relationship:[40,41]

$$\Theta_D = \frac{h}{k}\left(\frac{3}{4\pi V_a}\right)^{\frac{1}{3}} v_m. \quad (1)$$

Here, h, k, and V_a denote Planck's constant, Boltzmann's constant, and the atomic volume, respectively. v_m denotes the mean sound velocity v_m, which is determined from the averaged elastic constants of the material. Several calculation methods for averaging anisotropic C_{ij} were presented as reviewed in the literature.[42] We here numerically calculated the averaged-over-direction C_{ij} and s_{ij} by dividing the Euler angles and obtained the isotropic-approximation elastic constants from the averages between C_{ij} and $(s_{ij})^{-1}$. The determined Θ_D are given in Table II, together with the averaged-over-direction elastic moduli. The Debye temperature of β-Ga$_2$O$_3$ is significantly lower than those of the others because it contains heavy gallium, whereas Θ_D of θ alumina is the highest because it shows large bulk modulus and consists of light elements.

V. CONCLUSIONS

We determined the 13 (monoclinic-symmetry) elastic constants of β-Ga$_2$O$_3$ by performing resonant-mode identification through the RUS/LDI method. Density-functional-
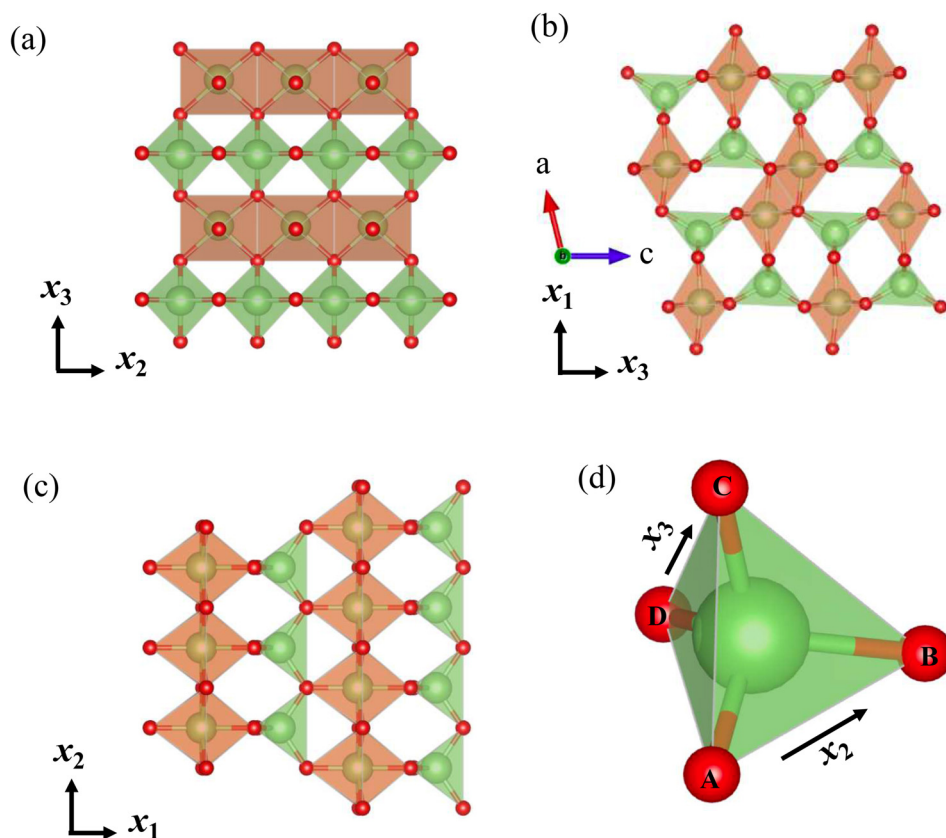
FIG. 5. Schematic projection views of the crystal structure on the (a) x_2–x_3, (b) x_1–x_3, and (c) x_1–x_2 planes. (d) An enlarged view of a tetrahedron in (a), whose two sides (AB and CD) align so as to be parallel to the x_2 and x_3 axes, respectively.
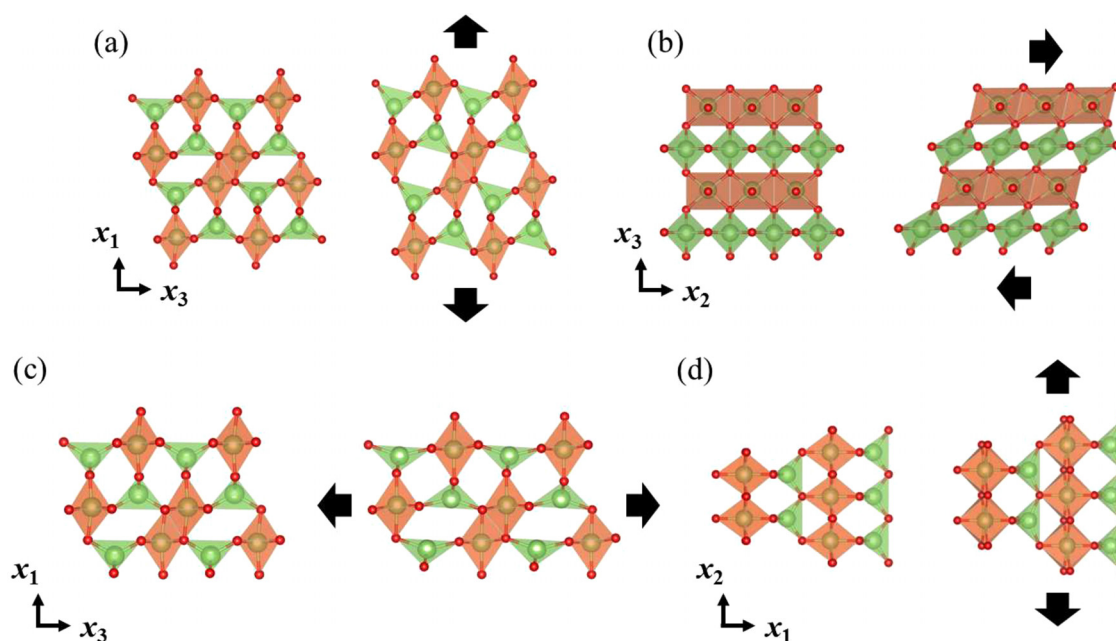

FIG. 6. Deformation behavior of β-Ga$_2$O$_3$ caused by (a) tensile strain along x_1 axis, (b) shear strain in the x_2–x_3 plane, (c) tensile strain along x_3 axis, or (d) tensile strain along x_2 axis calculated with the *ab-initio* calculation. The left and right images show the structures before and after applying the corresponding strain, respectively. Displacements of atoms are increased by 20 times.

theory calculation with the LDA potential provides both proper lattice constants and the elastic constants close to the measurements, indicating that other properties will be favorably predicted with this calculation method. β-Ga$_2$O$_3$ shows strong elastic anisotropies: It shows significantly low resistance to the longitudinal deformation along the x_1 axis and to the shear strain in the $x_2 - x_3$ plane, corresponding to small C_{11} and C_{44}. Unusual Poisson's ratios are found in β-Ga$_2$O$_3$ such as exceeding 0.5 and near-zero values. These anomalous elastic properties are consistently explained by focusing on the tetrahedra-octahedra crystallographic network, which is supported by the DFT calculation.

TABLE III. Changes in the neighboring Ga-O bond distance and the O-Ga-O bond angle calculated with the first-principles calculation, when the simple tensile or shear strain, corresponding to the diagonal elastic constants, is applied up to 1%.

Effective stiffness	Change ratio (%)	
	Distance	Angle
C_{11}	0.25	0.31
C_{22}	0.32	0.39
C_{33}	0.29	0.32
C_{44}	0.23	0.37
C_{55}	0.05	0.59
C_{66}	0.13	0.61

SUPPLEMENTARY MATERIAL

See supplementary material for FEM calculation of deformation of a tetrahedron.

ACKNOWLEDGMENTS

[1] V. M. Goldschmidt, T. F. W. Barth, and G. Lunde, Skr. Nor. Vidensk.-Akad., Oslo I. Mat. -Naturvidensk. Kl. **7**, 24 (1925).

[2] L. M. Foster and H. C. Stumpf, J. Am. Chem. Soc. **73**, 1590 (1951).

[3] J. A. Kohn, G. Katz, and J. D. Broder, Am. Miner. **42**, 398 (1957).

[4] S. Geller, J. Chem. Phys. **33**, 676 (1960).

[5] H. He, R. Orlando, M. A. Blanco, R. Pandey, E. Amzallag, I. Baraille, and M. Rérat, Phys. Rev. B **74**, 195123 (2006).

[6] E. G. Villora, K. Shimamura, T. Ujiie, and K. Aoki, Appl. Phys. Lett. **92**, 202118 (2008).

[7] J. B. Varley, J. R. Weber, A. Janotti, and C. G. Van de Walle, Appl. Phys. Lett. **97**, 142106 (2010).

[8] T. Onuma, S. Fujioka, T. Yamaguchi, M. Higashiwaki, K. Sasaki, T. Masui, and T. Honda, Appl. Phys. Lett. **103**, 041910 (2013).

[9] H. Peelaers and C. G. Van de Walle, Phys. Status Solidi B **252**, 828 (2015).

[10] F. Orlandi, F. Mezzadri, G. Calestani, F. Boschi, and R. Fornari, Appl. Phys. Express **8**, 111101 (2015).

[11] Z. Guo, A. Verma, X. Wu, F. Sun, A. Hickman, T. Masui, A. Kuramata, M. Higashiwaki, D. Jena, and T. Luo, Appl. Phys. Lett. **106**, 111909 (2015).

[12] M. Higashiwaki, K. Sasaki, A. Kuramata, T. Masui, and S. Yamakoshi, Appl. Phys. Lett. **100**, 013504 (2012).

[13] B. J. Baliga, J. Appl. Phys. **53**, 1759 (1982).

[14] S. L. Wang, J. W. Yu, P. C. Yeh, H. W. Kuo, L. H. Peng, A. A. Fedyanin, E. D. Mishina, and A. S. Sigov, Appl. Phys. Lett. **100**, 063506 (2012).

[15] J. W. Yu, P. C. Yeh, S. L. Wang, Y. R. Wu, M. H. Mao, H. H. Lin, and L. H. Peng, Appl. Phys. Lett. **101**, 183501 (2012).

[16] M. Higashiwaki, K. Sasaki, H. Murakami, Y. Kumagai, A. Koukitu, A. Kuramata, T. Masui, and S. Yamakoshi, Semicond. Sci. Technol. **31**, 034001 (2016).

[17] S. Krishnamoorthy, Z. Xia, S. Bajaj, M. Brenner, and S. Rajan, Appl. Phys. Express **10**, 051102 (2017).

[18] E. G. Villora, K. Shimamura, Y. Yoshikawa, K. Aoki, and N. Ichinose, J. Cryst. Growth **270**, 420 (2004).

[19] H. Aida, K. Nishiguchi, H. Takeda, N. Aota, K. Sunakawa, and Y. Yaguchi, Jpn. J. Appl. Phys., Part 1 **47**, 8506 (2008).

[20] J. P. Hebb and K. F. Jensen, IEEE Trans. Semicond. Manuf. **11**, 99 (1998).

[21] A. Toda, N. Ikarashi, H. Ono, S. Ito, T. Toda, and K. Imai, Appl. Phys. Lett. **79**, 4243 (2001).

[22] K. Ang, K. Chui, V. Bliznetsov, C. Tung, A. Du, N. Balasubramanian, G. Samudra, M. Li, and Y. Yeo, Appl. Phys. Lett. **86**, 093102 (2005).

[23] A. H. Heuer, A. Reddy, D. B. Hovis, B. Veal, A. Paulikas, A. Vlad, and M. Rühle, Scr. Mater. **54**, 1907 (2006).

[24] I. Koga, M. Aruga, and Y. Yoshinaka, Phys. Rev. **109**, 1467 (1958).

[25] R. T. Smith and F. S. Welsh, J. Appl. Phys. **42**, 2219 (1971).

[26] H. Ogi, K. Sato, T. Asada, and M. Hirao, J. Acoust. Soc. Am. **112**, 2553 (2002).

[27] H. Ogi, Y. Kawasaki, M. Hirao, and H. Ledbetter, J. Appl. Phys. **92**, 2451 (2002).

[28] H. Ogi, N. Nakamura, K. Sato, M. Hirao, and S. Uda, IEEE Trans. Ultrason. Ferroelectr. Freq. Control **50**, 553 (2003).

[29] H. Ogi, M. Fukunaga, M. Hirao, and H. Ledbetter, Phys. Rev. B **69**, 024104 (2004).

[30] H. Ogi, T. Ohmori, N. Nakamura, and M. Hirao, J. Appl. Phys. **100**, 053511 (2006).

[31] D. G. Isaak and I. Ohno, Phys. Chem. Miner. **30**, 430 (2003).

[32] E. Mochizuki, J. Phys. Earth **35**, 159 (1987).

[33] G. Kresse and J. Hafner, Phys. Rev. B **47**, 558 (1993).

[34] L. Fast, J. M. Wills, B. Johansson, and O. Eriksson, Phys. Rev. B **51**, 17431 (1995).

[35] K. Tanigaki, H. Ogi, H. Sumiya, K. Kusakabe, N. Nakamura, M. Hirao, and H. Ledbetter, Nat. Commun. **4**, 2343 (2013).

[36] A. Nagakubo, H. Ogi, H. Sumiya, K. Kusakabe, and M. Hirao, Appl. Phys. Lett. **102**, 241909 (2013).

[37] L. Levien, D. J. Weidner, and C. T. Prewitt, Phys. Chem. Miner. **4**, 105 (1979).

[38] J. Kandelin and D. J. Weidner, J. Geophys. Res. **93**, 1063, https://doi.org/10.1029/JB093iB02p01063 (1988).

[39] S. Shang, Y. Wang, and Z. Liu, Appl. Phys. Lett. **90**, 101909 (2007).

[40] M. Blackman, "Specific heat of solids," in *Handbuch Der Physik 7/1* (Springer, Berlin, 1955).

[41] O. L. Anderson, J. Phys. Chem. Solids **24**, 909 (1963).

[42] H. Ledbetter and S. Kim, *Handbook of Elastic Properties of Solids, Liquids, and Gases, Four-Volume Set 2* (Academic Press, 2000), Chap. 7.